metals

MDPI

Article

Investigation on Corrosion Resistance Properties of 17-4 PH Bound Metal Deposition As-Sintered Specimens with Different Build-Up Orientations

Pietro Forcellese [1], Tommaso Mancia [2], Michela Simoncini [2] and Tiziano Bellezze [1,*]

[1] Department of Materials, Environmental Sciences and Urban Planning, Polytechnic University of Marche, Via Brecce Bianche, 60131 Ancona, Italy; p.forcellese@pm.univpm.it
[2] Department of Industrial Engineering and Mathematical Science, Polytechnic University of Marche, Via Brecce Bianche, 60131 Ancona, Italy; t.mancia@staff.univpm.it (T.M.); m.simoncini@staff.univpm.it (M.S.)
* Correspondence: t.bellezze@staff.univpm.it; Tel.: +39-071-220-4413

Abstract: Additive manufacturing is a promising and emerging technology that can transform the global manufacturing and logistics by cutting costs and times of production. Localized corrosion resistance properties of 0°, 45°, and 90° build-up orientations of 17-4 PH as-sintered samples, manufactured by means of Bound Metal Deposition (BMD), have been investigated by electrochemical and morphological investigations. The cyclic potentiodynamic polarization curves and the open circuit potential monitoring, together with potential drop analysis, revealed that the BMD localized corrosion resistance properties were lowered if compared to a wrought 17-4 PH: a characteristic anodic behavior and many drops in potential were recorded for BMD, whilst the wrought specimens presented a typical passive behavior with pitting corrosion. Morphological investigations by scanning electron microscopy and energy-dispersive X-ray analysis revealed the presence of porosities and defects, especially for the 90° build-up orientation, and inclusions of SiO_2. The 45° build-up orientation showed the best corrosion resistance properties among all the BMD specimens, even though defects and porosities were observed, suggesting that their morphology and geometry influenced the overall corrosion behavior.

Keywords: localized corrosion; stainless steel; additive manufacturing; metal injection molding; Bound Metal Deposition; build-up orientations; SEM-EDX; cyclic potentiodynamic polarization; open circuit potential monitoring; potential drops analysis

Citation: Forcellese, P.; Mancia, T.; Simoncini, M.; Bellezze, T. Investigation on Corrosion Resistance Properties of 17-4 PH Bound Metal Deposition As-Sintered Specimens with Different Build-Up Orientations. *Metals* **2022**, *12*, 588. https://doi.org/10.3390/met12040588

Academic Editor: Amir Mostafaei

Received: 25 February 2022
Accepted: 25 March 2022
Published: 30 March 2022

1. Introduction

Additive manufacturing (AM) is the process that joints materials layer upon layer to make up objects from model data. The technology enables the fabrication of near-net-shaped artifacts with unique complex parts resulting in cost savings if compared to conventional manufacturing technologies [1].

The most relevant processes used for the AM of metallic alloys and steels are powder bed processes (PBP) and spray powder processes (SPP). In PBP, fine metal powders are layered and then sintered or melted with a laser or an electron beam to build up a part. In contrast with PBP, in SPP, fine metal powders are fed by a nozzle and melted with a laser or a plasma beam at room conditions or in an inert gas environment to reduce their oxidation [2]. Both the PBP and the SPP feedstock materials are metal powders, and the object is built up, adding layer-by-layer.

Stainless steel powders are conventionally obtained by means of water or gas atomization processes and are employed in AM as well as feedstock in powder metallurgy (PM) manufacturing processes, which consist of compacting, shaping, and sintering metal powders into near fully dense net-shaped parts [3]. Metal injection molding (MIM) is the PM technology that uses fine rounded metal powders, typically with average diameters up to

20 µm, combined with a binder, such as a thermoplastic polymer. In MIM processes, metal powders are shaped by means of a plastic injection molding machine at low temperatures, usually less than 200 °C; then, parts undergo the debinding through thermal, solvent, or catalytic erosion and finally they are sintered in an inert gas environment [3,4].

An emerging AM technology is Bound Metal Deposition™ (BMD) which is provided by Desktop Metal and is defined as "an extrusion-based metal additive manufacturing (AM) process where metal components are constructed by extrusion of a powder-filled thermoplastic media" [5]. Powders production, debinding, and consolidation processes of BMD are resemblant to those used for MIM; indeed, composites made up of fine metal powders mixed with a polymer–wax binder are employed as feedstock. The composite material is printed layer upon layer on a build plate and then manufacts undergo debinding and sintering processes. Manufacts come with non-structural parts made of composite material, in particular supports and the filler of the blank parts. The separation of the non-structural parts of an artifact is performed by the Ceramic Release Layer™ (CRL), a composite material of ceramic particles embedded in a polymer–wax binder that is removed during the debinding process [6].

The BMD stainless steels have been printed to produce jigs, fixtures, tooling, and molds in automotive, space, defense, medical, and prototyping fields, demonstrating costs and time savings compared to conventional manufacturing processes [7–10].

Theoretically, BMD stainless steels can be assimilated to MIM, in terms of mechanical and corrosion resistance properties, even though the BMD have been limitedly investigated in scientific literature, to the best of the present authors' knowledge. The MIM stainless steels can reach densities of 95–97%, and mechanical properties are close to wrought materials; nevertheless, residual porosities, oxides inclusions, and carbon content can heavily affect both mechanical and corrosion resistance properties [11,12].

In this work, preliminary corrosion resistance investigations of as-sintered 17-4 PH BMD samples with different build-up orientations were investigated by means of cyclic potentiodynamic polarization (CPP) anodic curves and long-term open circuit potential (OCP) monitoring in NaCl solutions. The morphological and chemical characterization of the investigated samples were carried out by means of optical microscopy (OM) observations, spectrometry, and scanning electron microscopy (SEM) together with energy dispersive X-ray (EDX) analysis [13]. The samples were fabricated in three orientations with respect to the build plate of the printer: 0°, 45°, and 90°. Wrought 17-4 PH corrosion resistance properties were assessed too, as material and manufacturing technology references.

2. Materials and Methods

The material 17-4 PH is a martensitic stainless steel whose typical grain structure can be obtained by heat treatment of 1 h of solubilization at 1040 °C followed by ageing for 1 h at 482 °C [14]. The feedstock of mixed metal powders and binder used in this study is commercialized as 17-4 PH by Desktop Metal, and investigated manufacts consisted of as-sintered material, whose martensitic microstructure could be theoretically granted by the cooling rates commonly given in the sintering process [15,16].

Samples of 17-4 PH as-sintered BMD were fabricated by means of a Studio System™ with three different build-up orientations of 0°, 45°, and 90°. A schematic representation of the build-up orientations of the layer-by-layer printing process is given in Figure 1.

A Studio System™ is made up of a printer, a debinding chamber, and a sintering furnace. The extruder nozzles of the metal powders mixed with binder and the CRL used in this study were 0.4 mm diameter, whereas the extruded layer thickness was set to 0.1 mm. After printing, the parts undergo debinding for 30–40 h, assisted by trans-1,2 dichloroethylene, a nonpolar solvent recovered during the process. Since the polymer–wax binder is removed, the resulting parts are brittle, and then sintering is required to obtain a manufact having functional and structural properties. Sintering was performed up to 40 h in a furnace with mixture of 97% argon and 2.9% hydrogen. The 17-4 PH as-sintered BMD specimens were 25 × 25 × 3 mm plates, as Figure 2 shows.

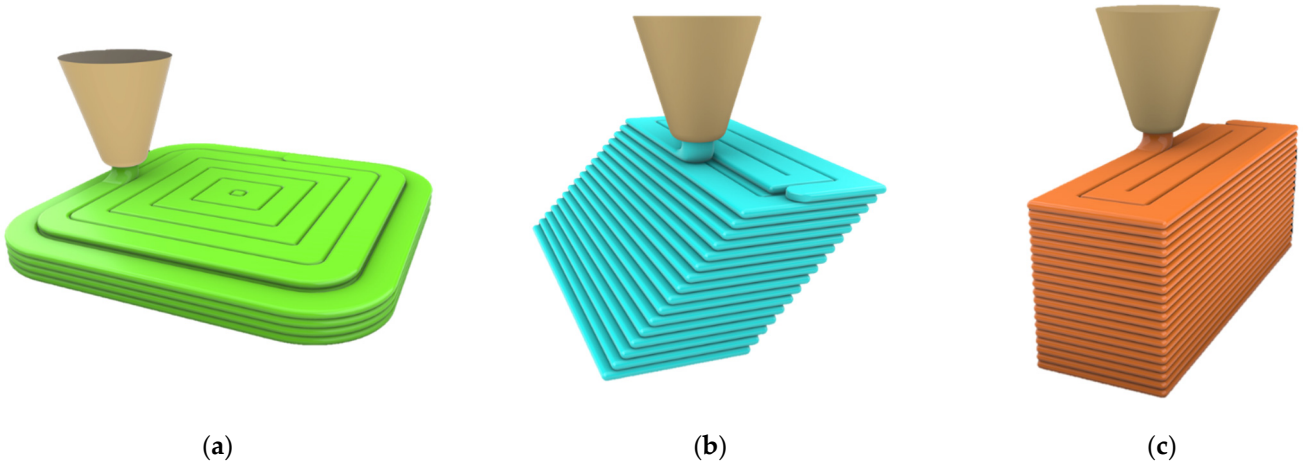

(**a**) (**b**) (**c**)

Figure 1. Build-up orientations: (**a**) 0°; (**b**) 45°; (**c**) 90°.

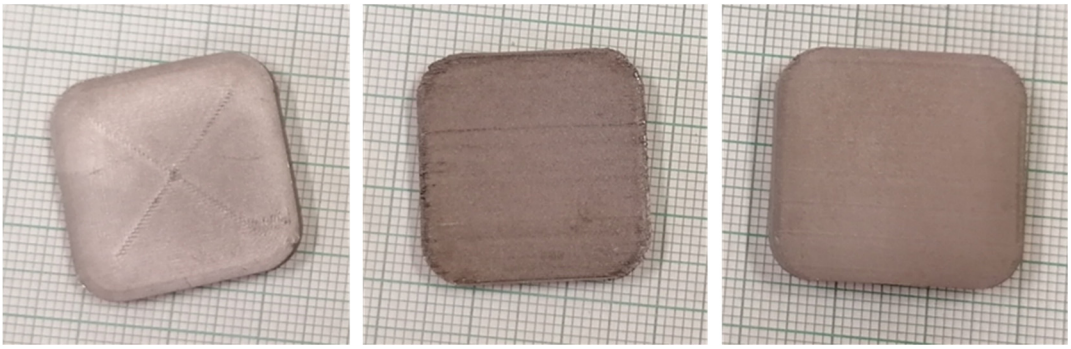

(**a**) (**b**) (**c**)

Figure 2. The 17-4 PH BMD as-sintered plate specimens: (**a**) 0°; (**b**) 45°; (**c**) 90°.

Before corrosion tests, the sample preparation was carried out by embedding the plates in acrylic resin and grinding their surfaces up to 1200 grit by a lapping machine; then, the specimens were sonicated in deionized water for 5 min and in n-hexane for 15 min. Samples were then dried with hot air and rested for one night before performing other assessments, with the aim of promoting the protective passive film layer growth and the evaporation of residual traces of n-hexane.

Concerning the CPP and long-term OCP analysis, a protective and adhesive polyimide tape with a circular area of 1.23 cm^2 was applied with the aim of limiting the surface exposed to the electrolyte testing solution. In CPP tests, the specimen was first immersed for 30 min in the electrolyte solution and OCP was recorded during this period until an almost stationary value was reached. Then, electrochemical impedance spectroscopy (EIS) measurements were performed in a range of frequencies from 100 kHz to 1 Hz to estimate ohmic loss due to testing solution resistance for the correction of the CPP curves. Polarization curves were taken afterwards with a scan rate of 83 $\mu V \cdot s^{-1}$, starting from a potential 175 mV more negative than stationary OCP and going towards positive potentials until the current density reached 0.1 $mA \cdot cm^{-2}$; then, the scan was reversed until current densities were close to those of passivation conditions, recorded during the forward scan. The CPPs were performed with a Gamry Reference 600 potentiostat/galvanostat in an electrochemical cell with three-electrodes configuration: 17-4 PH specimens as the working electrode, activated titanium wire as the counter electrode, and saturated calomel electrode (SCE, E = 0.241 V vs. SHE) as the reference electrode. Electrolyte solution used in CPP and EIS analyses was 0.35 wt% NaCl. Corrosion resistance behavior of BMD samples was assessed by Gamry Echem Analyst software, applying the Tafel fit on CPP curves, which estimates the corrosion current densities (i_{corr}) of the curve. The i_{corr} of BMD curves was

also assessed by the extrapolation of the current density by crossing the cathodic linear part of the curve at the potential equal to corrosion potential (E_{corr}), for comparison with values obtained by Tafel fit [17]. Three tests were performed for each sample with a different build-up orientation.

The corrosion resistance properties were also assessed by means of OCP recording for 108 h in a long-term exposure of BMD and wrought samples placed together into a cell of 25 L filled with stronger solution of NaCl 3.5 wt%, compared to the test solution used for CPP curves, to enhance the corrosion process. The long-term OCPs monitoring were performed using an SCE as reference electrode and an Agilent Data Switching Unit Mod. 34970A with a multiplexer module 34901A. Three tests were performed for each sample with a different build-up orientation.

The chemical composition of the as-sintered BMD was analyzed by means of spark spectrometer Spark Analyzer Spectrolab.

Morphology of 17-4 PH BMD surfaces was investigated with SEM-EDX analysis by means of Zeiss FE-SEM SUPRA 40 performed on 0°, 45°, and 90° samples.

The corrosion effects induced by electrochemical tests on the surface area of BMD specimens were evaluated by OM afterwards, recording the CPP curves.

3. Results and Discussion

The chemical composition of 17-4 PH BMD is reported in Table 1, compared to that provided by Desktop Metal technical datasheet.

Table 1. Chemical composition of 17-4 PH BMD compared to Desktop Metal reference values.

	% C	% Si	% Mn	% Cr	% Ni	% Al	% Cu	% Nb + Ta
17-4 PH BMD	0.03	2.09	0.45	16.9	4.62	0.01	1.71	//
Desktop Metal reference values	0.07 (max)	// [1]	<1.0	15.5–17.5	3–5	// [1]	3–5	0.15–0.45

[1] Not reported.

All the percentage values of 17-4 PH BMD specimens are in the range of given reference values reported in Desktop Metal technical datasheet, except for copper which is below the reported threshold.

Despite that silicon concentration is not reported in reference values, it was found significantly higher in the BMD than in wrought 17-4 PH [14]. Since it has high mobility and a greater affinity to oxygen among the other alloying elements, higher concentrations of silicon are typical for stainless steels powders to prevent the formation of other, more detrimental oxides during the water atomization process [18–21].

SEM images of grinded BMD samples before corrosion tests, illustrated in Figure 3, show that the bulk surface morphology is significantly different compared to the characteristic morphology of wrought specimens, which disclosed a fully dense material (not shown for the sake of brevity). On the contrary, all the three build-up orientations of the BMD samples show porosities and defects, indicated by red arrows in Figure 3.

Such imperfections can be barely observed in 0° build-up orientation and are mostly present in the form of shallow defects. In 45° they are deeper, their density increases, and a few porosities can be observed, too. The most affected specimen is the 90° build-up orientation; indeed, many fissure-shaped hollows of 10 µm wide in the maximum opening can be recognized. Porosities are oriented in the same pattern and direction followed by the printing nozzle for each build-up orientation, suggesting that layer-by-layer deposition led to such imperfections.

Surfaces and then the bulk of all the BMD specimens contained abundant SiO_2 inclusions in a wide range of sizes and shapes, as illustrated by the dark particles embedded in the investigated area, as Figures 3 and 4 show. EDX results for an examined dark particle on a 90° surface area specimen are given in Table 2.

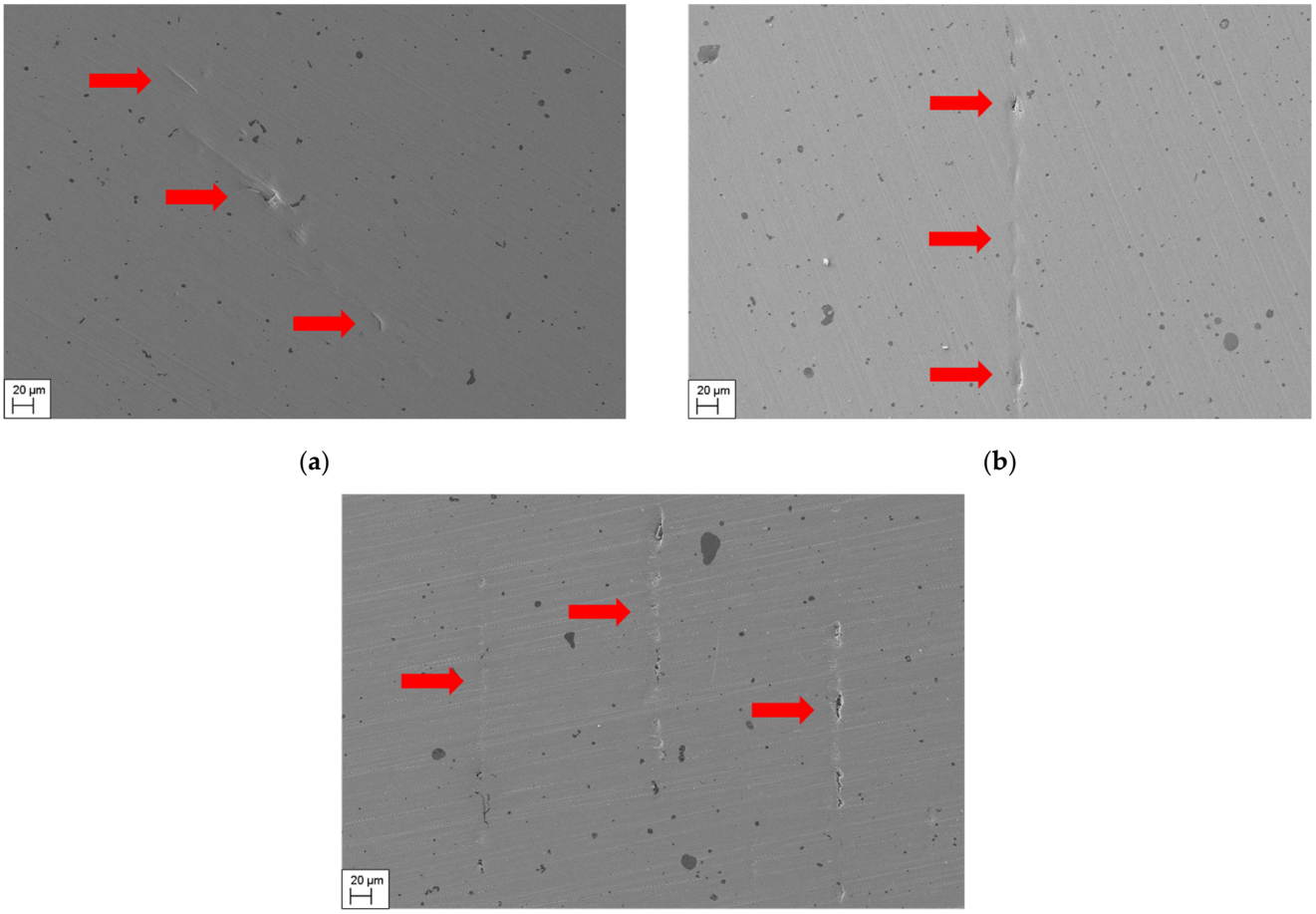

(**a**) (**b**)

(**c**)

Figure 3. SEM images of the surface area of 17-4 PH BMD specimens: (**a**) 0°; (**b**) 45°; (**c**) 90°. Red arrows point at porosities and defects.

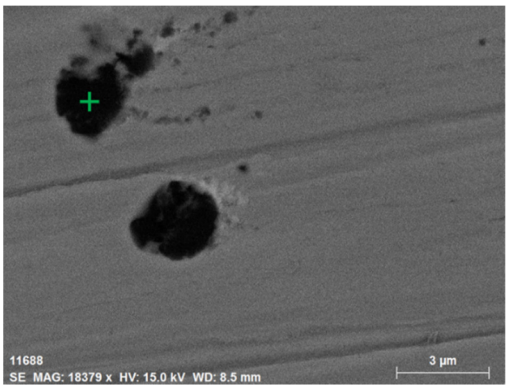

Figure 4. SEM-EDX acquisition of a SiO_2 inclusion on a 90° specimen.

Table 2. Atomic percentage of SiO_2 inclusion of Figure 4 (green symbol).

% O	% Si	% C	% Fe	% Cr	% Cu	% Ni
51.6	26.0	14.5	5.26	2.2	0.4	0.1

Silica particles may form during both water atomization and sintering processes; indeed, inclusions of SiO_2 particles have been reported on the surface of metal powders as well as on sintered stainless steels [22–24]. Their presence has been attributed to low

dewpoint (high residual water content in the sintering chamber), to low sintering or atomization process temperature, or to reoxidation processes which can occur for slow cooling rates of sintering or atomization [19,22,25]. However, it is not possible to totally avoid the formation of SiO_2 inclusions due to the high oxygen affinity and its difficulty to reduction in the sintering furnace [3].

The CPP curve recorded for a 17-4 PH wrought martensitic stainless steel in a solution of NaCl 0.35 wt% is plotted in Figure 5.

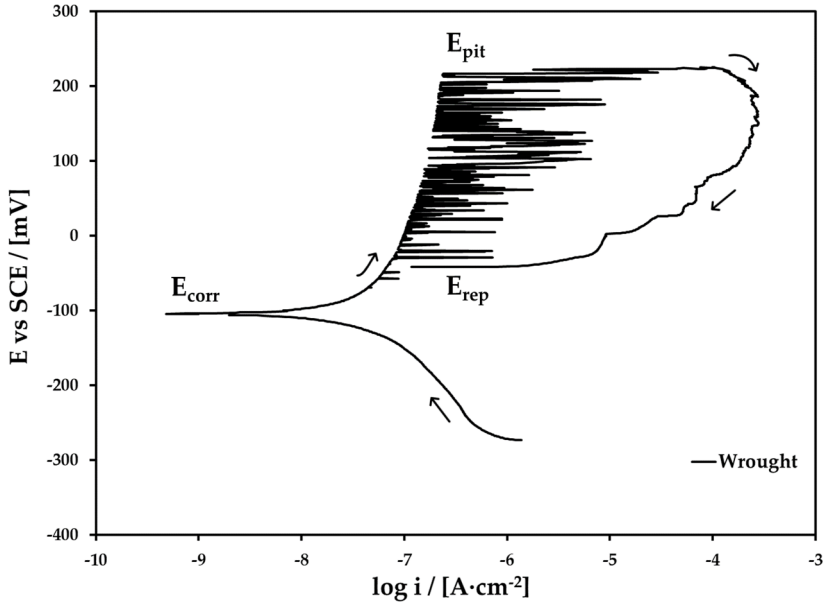

Figure 5. CPP curve of 17-4 PH wrought stainless steel sample in NaCl 0.35 wt%. Arrows point at the direction of the scan.

The polarization curve is representative of a passive film on a stainless-steel alloy with many metastable pit events and a visible negative hysteresis after the inversion of the potential scan. Corrosion potential, pitting potential (E_{pit}), and repassivation potential (E_{rep}) were found, respectively; E_{corr} = −105 mV, E_{pit} = 220 mV, and E_{rep} = −45 mV.

Corrosion resistance properties of MIM stainless steels, comparable with the BMD studied in this work, have been assessed with many techniques such as immersion testing, salt spray test, electrochemical potentiokinetic reactivation, stepwise polarization, and OCP and CPP too [20,26–33]. Electrochemical tests as CPP curves are usually employed to assess the localized corrosion of wrought stainless steel, even though the interpretation of polarization curve data can be difficult due to the presence of oxides, defects, and porosities of MIM materials [3]. Considering the good reproducibility of the recorded experimental CPP curves, the most representative of 0°, 45°, and 90° 17-4 PH as-sintered BMD samples are plotted in Figure 6.

The presence of defects, porosities, and oxide particles (Figure 3) can lower the localized corrosion resistance of the 17-4 PH BMD, if compared with the wrought specimens, most likely to micro-crevice corrosion processes. In addition, crevice corrosion can occur near the borders of the surface area exposed to the electrolyte test solution [19,22,34–36].

None of the CPP curves of each specimen showed up a typical passive region for a stainless steel tested in a neutral chloride solution, or limitedly present for 0° specimen (red curve in Figure 6). For this reason, the determination of a characteristic localized corrosion potential of the curves was difficult, both in the case of pitting and crevice processes, in contrast with that determined for the curve in Figure 5. After the inversion of the potential scan, the 0° specimens showed a negative hysteresis, leading to a E_{rep} close to the E_{corr}, meaning that passivation conditions are likely present in this sample and were restored despite the curve forward trend. Moreover, its corrosion potential and

corrosion current are comparable to those of a stainless steel, similar to that corresponding to the wrought 17-4 PH of Figure 5 (10^{-7}–10^{-6} A·cm^{-2}). The 90° samples also exhibited a negative hysteresis after the potential scan inversion, but E_{rep} was found approximately 50–100 mV below E_{corr} (green curve in Figure 6), indicating that this type of sample is considerably not able to repassivate with risk of localized corrosion attacks on the surface exposed to the chloride solution. Surprisingly, the CPP of the 45° specimens gives a slight positive hysteresis of the curve, with E_{rep} higher than E_{corr}. Despite that SEM images of Figure 3b revealed more defects and porosities than the 0°, the CPP of the 45° specimens (blue curve in Figure 6) suggests that this build-up orientation has better corrosion behavior under anodic polarization among the different BMD specimens.

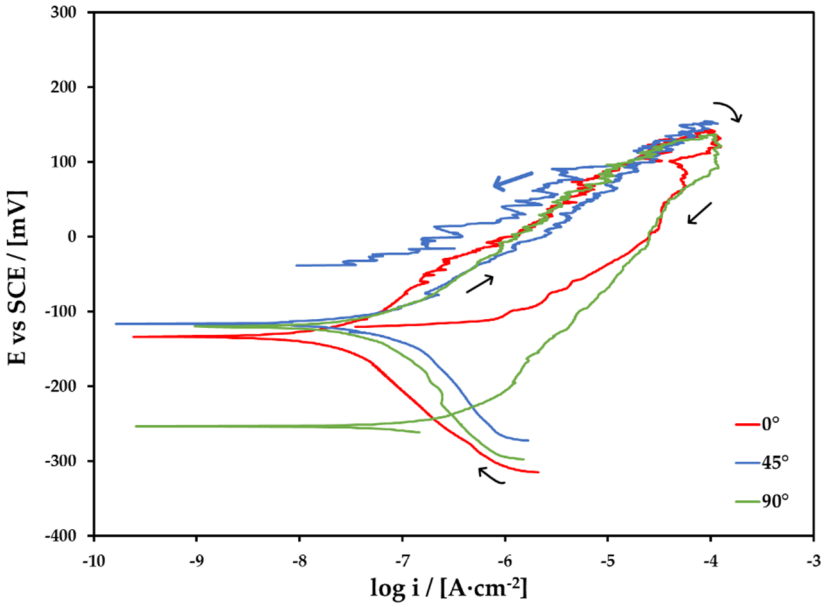

Figure 6. CPP curves of 17-4 PH BMD stainless-steel samples 0° (red), 45° (blue), and 90° (green) build-up orientations. Arrows point at the direction of the scan.

Considering that the observed 17-4 PH BMD anodic branches effectively showed a trend similar to that of "active metals", a Tafel fit model was used for analyzing the experimental data of the curves. Mean values with standard deviations of E_{corr} and i_{corr} obtained from Tafel fit are reported in Table 3. This table also reports the values of i_{corr} determined by extrapolation method of the cathodic branch at E_{corr} value, as proposed by other authors applying this method for stainless steel in chlorides neutral testing solutions [17]. The results of this analysis are given to compare the results obtained from the Tafel fit procedure.

Table 3. CPP, Tafel fit, and cathodic extrapolation results.

Build-Up Orientation	E_{corr} [mV]	σ	i_{corr} (Tafel Fit) [μA·cm^{-2}]	σ	i_{corr} (Extrapolation) [μA·cm^{-2}]	σ
0°	−124	10	0.044	0.004	0.030	0.006
45°	−126	9	0.119	0.004	0.105	0.008
90°	−137	17	0.146	0.036	0.090	0.048

Values of E_{corr} are similar for all the BMD specimens and are close to a wrought martensitic stainless steel (comparing Figures 5 and 6) and are representative of the presence of a homogeneous passive film layer. More specifically, E_{corr} of the wrought 17-4 PH was found to be −105 mV, which is slightly more noble than those of BMD samples, hence the passive layer of these specimens could be less homogeneous due to the presence of the

observed defects and porosities (Figure 3). However, i_{corr} mean values of BMD calculated both from Tafel fit and cathodic extrapolation range between 0.04–0.15 × 10^{-6} A·cm^{-2} (Table 3) and are comparable to the current density of the wrought material passivation range, which is 10^{-7}–10^{-6} A·cm^{-2} (Figure 5), indicating that most of the surface of the BMD specimens is fairly protected against localized corrosion, similar to the wrought counterpart. These observations allow to conclude that the 17-4 PH BMD samples are in a passive state, although the apparently "active behavior" of these specimens, as per their anodic branches of Figure 6, apparently suggest the contrary.

OM images revealed that most of the exposed surface area was unaffected by localized corrosion after CPP curve acquisition, except for the attacks along the border of the polymeric tape-shielded areas and inside porosities, as illustrated in Figure 7.

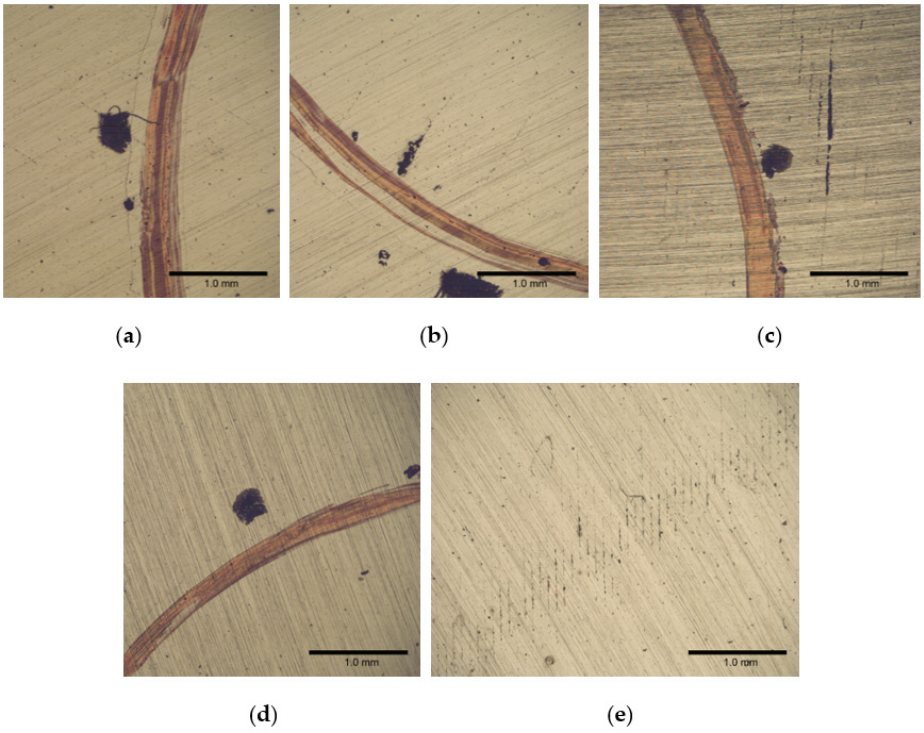

Figure 7. OM images of 17-4 PH BMD specimens: (**a**,**b**) 0°; (**c**) 45°; (**d**,**e**) 90°. Red lines were signed after CPP to underline the border of the exposed area to the testing solution.

Traces of localized corrosion can be recognized along the borders of each BMD samples (Figure 7a,c,d) and inside some porosities of the exposed surface area of 0° and 90° specimens, respectively (Figure 7b,e). Morphology of the injury produced by corrosion was peculiar of each sample; indeed, for the 0° build-up the corrosion sometimes produced a damage close to crevice inside or near porosities, whilst the 90° surfaces were abundant in porosities (Figure 3c), which resulted as slightly heightened after the CPP, as expected due to higher negative hysteresis (green curve in Figure 6). The images of 45° specimens revealed that no signs of localized corrosion attacks can be appreciated in the exposed surface area, but still signs of localized corrosion were found over the border of the shielded area, as shown in Figure 7c. The localized corrosion attacks confirmed that corrosion resistance is lowered if compared to a wrought material, and the crevice corrosion processes are prevailing. OM analysis also suggests that after the CPP the 0° and 45° specimens suffered less or no damage, respectively, compared to 90° specimens.

The comparison of the localized corrosion behavior among BMD specimens themselves and with respect to wrought specimen, according to the results obtained from CPP curves and Tafel fit, suggests that electrochemical anodic polarization supplies interesting information, although it cannot be considered as completely reliable, considering the observed singular anodic behavior of the BMD specimens. Therefore, OCP monitoring

was performed for supplying additional information on the passive film formation and the corrosion behavior of the stainless steel samples over time.

The OCP of 17-4 PH BMD 0°, 45°, and 90° and of the wrought specimens were monitored for 108 h in a NaCl 3.5 wt% solution to accelerate the corrosion rates. The curves illustrated in Figure 8 are the most representative of each specimen, considering the good reproducibility of the experimental OCP curves.

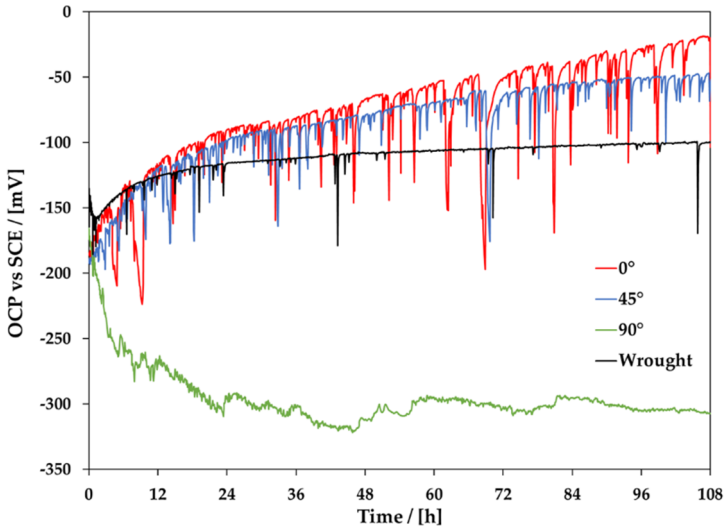

(**a**)

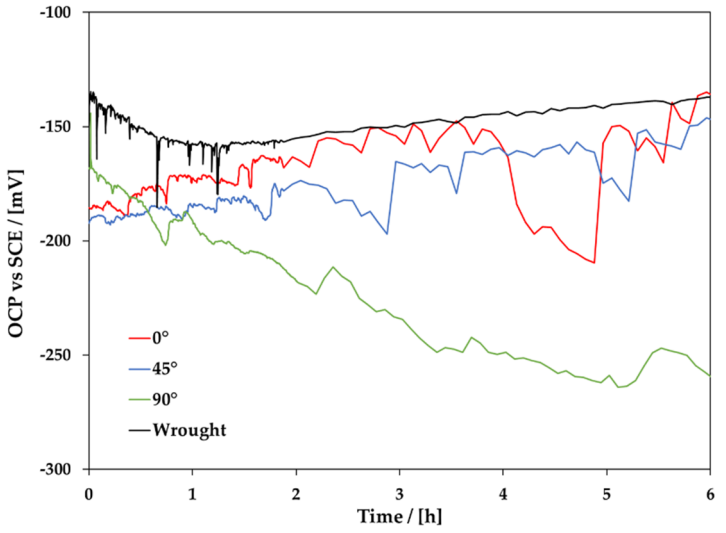

(**b**)

Figure 8. OCP of 0°, 45°, and 90° build-up orientations and wrought 17-4 PH specimens: (**a**) 108 h OCP monitoring; (**b**) enlargement of the first 6 h of OCP monitoring.

Afterwards, approximately 2 h from the immersion in the testing solution, the wrought 17-4 PH systematically presented a positive trend of the OCP vs. SCE, with few drops towards active potentials lasting up to 5–10 min (Figure 8b). In addition, 0° and 45° samples had a positive trend of the curves, even though drops in potential were significantly higher in number, time width, and potential drop. The 90° specimen showed a negative trend since the beginning of the experiment, indicating that the corrosion process starts in the early stage of the exposure to the corrosive solution. Visible signs of corrosions appeared in the 90° specimens after only 12–24 h from the immersion, whilst no corrosion products

or damage were observed for 0°, 45°, and wrought specimens, nor by OM image analysis. Corrosion products found on the surface of 90° specimens are illustrated in Figure 9.

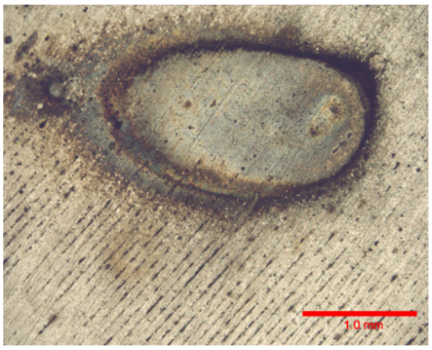

Figure 9. OM image of corrosion products on 90° sample after the OCP investigation.

Concerning 0°, 45°, and wrought OCP curves, a logarithmic baseline of data was reconstructed between 6 and 102 h by means of nonlinear regression of the points considered as the baseline of each curve; these points were selected applying thresholds to the curve derivative and then to the OCP curve itself. Then, potential drops higher than 10 mV from the baseline were detected in number, time width, and potential drop peaks by numeric procedure. Graphs plotted in Figure 10 display the results of this procedure; in particular, red dots highlight the minimum of each potential drop peak detected during OCP monitoring.

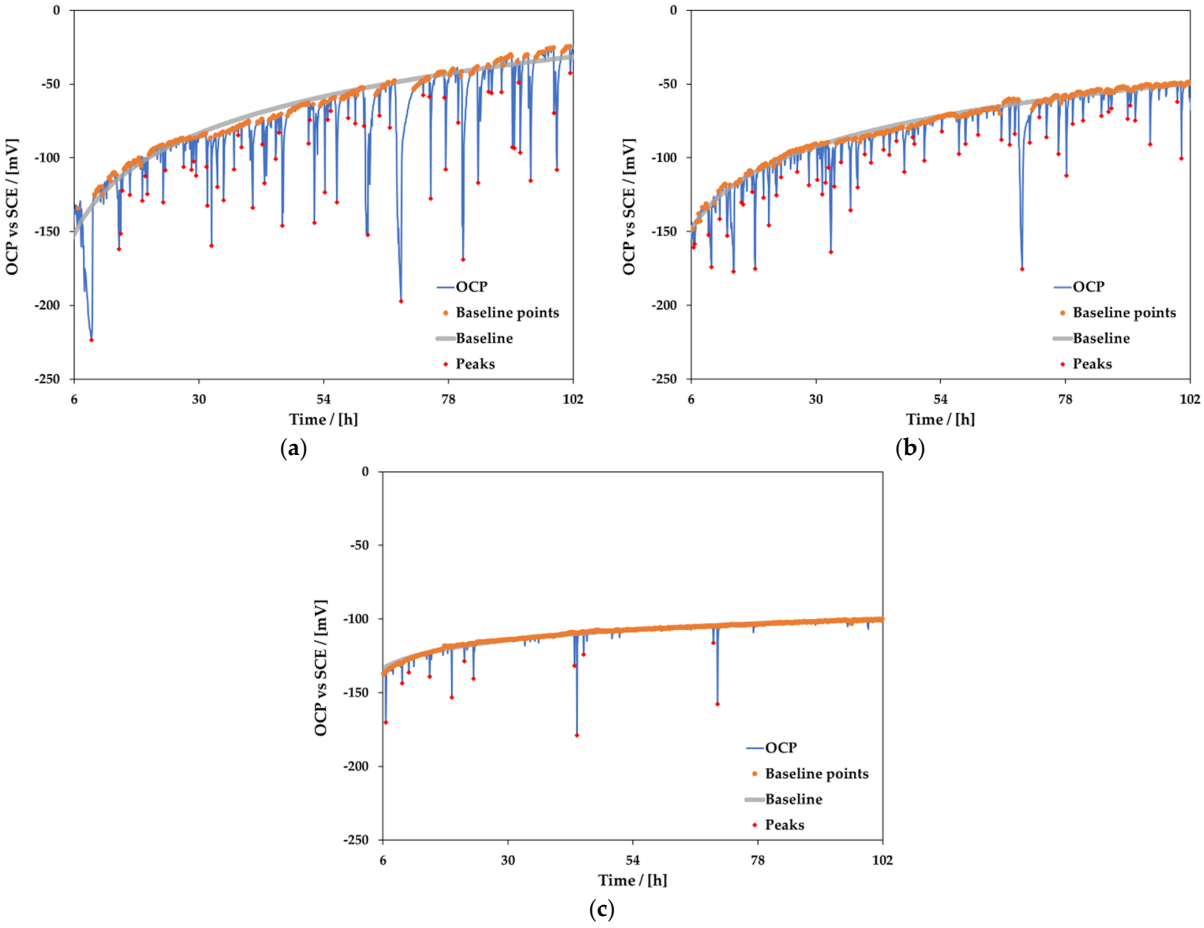

Figure 10. Potential drops analysis of the OCP curves: (**a**) 0°; (**b**) 45°; (**c**) wrought.

The wrought 17-4 PH specimens exhibited more abundant drops in 24–30 h, then the curve seems to stabilize in drops and slope of the curve (Figure 10c). Concerning the logarithmic baselines of 0° and 45° specimen curves, respectively Figure 10a,b, they were comparable to each other, and they were nobler than the baseline of wrought specimen curves. In the BMD curves, the potential drops toward negative values and then toward active potentials may be attributed to the presence of defects, porosities, and inclusions (Figure 3).

In Table 4 are listed the calculated parameters chosen to compare 0°, 45°, and wrought specimens: the total number, the cumulative time width, and the cumulative "negative peak intensity" or simply "intensity" of potential drops. The intensity is meant as the absolute area of a OCP negative peak, approximately considered as a triangle with the base equal to the time width and the height equal to the potential drop from the baseline.

Table 4. Results of potential drops analysis.

Sample	Total Number of Drops	σ	Cumulative Time Width [h]	σ	Cumulative Intensity [mV·h]	σ
0°	65	3.5	24.15	1.73	965.2	92.5
45°	65	4.5	15.79	2.87	420.4	133.5
Wrought	9	3	0.83	0.25	11.5	4.0

The potential drops analysis revealed that the passive film of the wrought sample was significantly more stable than the BMD specimens in the corrosive test solution; thus, few small negative peaks lasting up to 10 min were recorded. Despite that the mean value of the total number of drops of BMD samples was the same, the cumulative time width and intensity were significantly different, indicating that the passive film on the 45° build-up surface is more stable and efficient against localized corrosion when compared to that of the 0° specimens. Higher values for time width and potential drop from the baseline were recorded in the populations of negative peaks found in the 0° specimen, indicating that the tendency to move towards active potentials is higher than 45°.

Coupled OCP and CPP analysis, respectively, in a weak and a strong neutral chloride test solution, produced reliable data to evaluate corrosion resistance properties of 17-4 PH BMD specimens in different build-up orientations.

The potential drops analysis of the OCP curves (Figure 8) confirms results obtained by means of CPPs (Figures 5 and 6). A pure passive behavior and $E_{rep} > E_{corr}$ (material operating in the perfect passivity region) of the wrought specimens correspond to a limited presence of potential drops in the OCP curves [13,37]. The hysteresis of the CPP curve of 0° specimens together with an E_{rep} close to E_{corr} (material limitedly able to repassivate), and the positive hysteresis with $E_{rep} > E_{corr}$ in CPP curves of 45° samples (material able to remain passive), can be compared to higher values of "cumulative time width" and "cumulative peak intensity" (Table 4) of the 0° with respect to the 45° build-up orientation. Finally, a large negative hysteresis and $E_{rep} < E_{corr}$ in 90° CPP curves (material unable to repassivate) corresponds to its tendency to move towards active potentials and to clearly show corrosion products (Figure 9) in the early stage of the OCP test.

Given this correspondence, CPP curves seem a reliable short-term electrochemical tool to access the localized corrosion of the investigated BMD samples, at least in this preliminary investigation. Their characteristic anodic behavior could be attributed to the presence of defects, porosities, and inclusions introduced by BMD processes, which lower the overall corrosion resistance properties when compared with those of pure passive stainless steel, such as wrought material. Considering the printing orientation, the 45° build-up samples showed the best localized corrosion resistance, suggesting that the internal geometry and morphology of porosities and defects may play a role in the corrosion behavior, too.

4. Conclusions

In this work, localized corrosion resistance and morphology of 17-4 PH as-sintered BMD stainless steel with different build up-orientations (0°, 45°, and 90°) were assessed by means of CPP, OCP, OM, and SEM-EDX analyses and compared to a wrought 17-4 PH stainless steel.

The morphology of BMD grinded specimen surfaces revealed the presence of defects and porosities in the bulk material that can be attributed to the layer-by-layer printing process. The 90° specimens were the most affected, whilst 0° and 45° specimens resulted in less abundant and pronounced defects.

The typical passive region of a stainless steel CPP curve was not observed for any of the 17-4 PH BMD specimens, even though their corrosion current densities were comparable to the passivation current density of a wrought 17-4 PH stainless steel (10^{-7}–10^{-6} A·cm^{-2}). This result suggests that BMD specimens are fairly protected against localized corrosion, and they are in a passive state, although the characteristic localized corrosion potential (related to pitting and/or crevice corrosion) cannot be identified in the CPP curves. On the other hand, the repassivation properties of BMD specimens has been analyzed, showing that 45° specimens showed better behavior compared to 0°, and, in particular, to 90° specimens. These results were in accordance with the specimen morphology observations.

The OCP curves of 90° specimens resulted in a trend towards active potentials, together with the observation of corrosion products on the surface. Contrarily, 45° and 0° specimens showed increasing OCP trends with several potential drops towards negative potentials. Their cumulative analysis, in terms of time width and intensity, revealed that the passive film of the 45° surfaces resulted in more efficiency against localized corrosion and stability compared to that of the 0° specimens. These results confirm the conclusions given by the CPP curves.

Finally, considering that the acquisition time of CPP curves is shorter than that of OCP curves, they seem to be a reliable electrochemical tool to access the localized corrosion behavior of BMD specimens, at least in this preliminary investigation.

Author Contributions: Conceptualization, P.F. and T.B.; methodology, P.F. and T.B.; software, P.F. and T.B.; investigation, P.F.; resources, P.F., T.M., M.S. and T.B.; data curation, P.F. and T.B.; writing—original draft preparation, P.F.; writing—review and editing, T.M., M.S. and T.B.; supervision, M.S. and T.B. All authors have read and agreed to the published version of the manuscript.

Funding: This research received no external funding.

Data Availability Statement: Not applicable.

Acknowledgments: The authors wish to thank Filippo Bonora for the support provided during this research activity.

Conflicts of Interest: The authors declare no conflict of interest.

References

1. Frazier, W.E. Metal additive manufacturing: A review. *J. Mater. Eng. Perform.* **2014**, *23*, 1917–1928. [CrossRef]
2. Yakout, M.; Elbestawi, M.A.; Veldhuis, S.C. A review of metal additive manufacturing technologies. *Solid State Phenom.* **2018**, *278*, 1–14. [CrossRef]
3. Klar, E.; Samal, P.K. *Powder Metallurgy Stainless Steels: Processing, Microstructure, and Properties*; ASM International: Materials Park, OH, USA, 2007. [CrossRef]
4. Petzoldt, F.; Hartwig, T. Overview on binder and feedstock systems for PIM. In Proceedings of the Second European Symposium on Powder Injection Molding, Munich, Germany, 18–20 October 2000; pp. 43–50.
5. Desktopmetal.com. Available online: https://www.desktopmetal.com/resources/deep-dive-bmd (accessed on 22 February 2022).
6. Watson, A.; Belding, J.; Ellis, B.D. Characterization of 17-4 PH processed via bound metal deposition (BMD). In Proceedings of the TMS 2020 149th Annual Meeting & Exhibition Supplemental Proceedings, Pittsburgh, PA, USA, 12 February 2020; pp. 205–216.
7. Desktop Metal. *Case Study: Alpha Precision Group*; Desktop Metal: Burlington, MA, USA, 2020; pp. 1–12.
8. Desktop Metal. *Case Study: Egar Tool & Die Ltd.*; Desktop Metal: Burlington, MA, USA, 2020; pp. 1–11.
9. Desktop Metal. *Case Study: Innovative Plastics*; Desktop Metal: Burlington, MA, USA, 2020; pp. 1–7.

10. Desktop Metal. *Case Study: Lumenium*; Desktop Metal: Burlington, MA, USA, 2018; pp. 1–7.
11. Mascerahanas, J.; Schlieper, G. High strength MIM materials. In Proceedings of the Second European Symposium on Powder Injection Molding, Munich, Germany, 18–20 October 2000.
12. Torralba, J.M.; Hidalgo, J. Metal injection molding (MIM) of stainless steel. In *Handbook of Metal Injection Molding*; Woodhead Publishing Series in Metals and Surface Engineering; Heaney, D., Ed.; Woodhead Publishing: Cambridge, UK, 2019; pp. 409–429.
13. Bellezze, T.; Giuliani, G.; Roventi, G. Study of stainless steels corrosion in a strong acid mixture. Part 1: Cyclic potentiodynamic polarization curves examined by means of an analytical method. *Corros. Sci.* **2018**, *130*, 113–125. [CrossRef]
14. Bellezze, T.; Roventi, G.; Fratesi, R. Localised corrosion and cathodic protection of 17 4PH propeller shafts. *Corros. Eng. Sci. Technol.* **2013**, *48*, 340–345. [CrossRef]
15. Svilar, M.; Ambs, H.D. PM Martensitic stainless steels: Processing and properties. *Adv. Powder Metall. Part. Mater.* **1990**, *2*, 259–272.
16. Reinshagen, J.H.; Witsberger, J.C. Properties of precipitation hardening stainless steel produced by conventional powder metallurgy. *Adv. Powder Metall. Part. Mater.* **1994**, *7*, 7–339.
17. Costa, I.; Franco, C.V.; Kunioshi, C.T.; Rossi, J.L. Corrosion resistance of injection-molded 17-4PH steel in sodium chloride solution. *Corrosion* **2006**, *62*, 357–365. [CrossRef]
18. Reinshagen, J.; Neupaver, A. Principles of atomization. *Phys. Chem. Powder Met. Prod. Process.* **1989**, 16. Available online: https://www.beyonddiscovery.org/powder-metallurgy/references-mtj.html (accessed on 22 February 2022).
19. Ro, D.H.; Klar, E. Corrosion behavior of P/M austenitic stainless steels. *Mod. Dev. Powder Metall.* **1980**, *13*, 247–287.
20. Larsen, R.M.; Thorsen, K.A. Removal of oxygen and carbon during sintering of austenitic stainless steels. In Proceedings of the PM World Congress, Kyoto, Japan, 12–15 July 1993.
21. Ferris, D.P. Surface analysis of steel powders by ESCA. *Int. J. Powder Met. Powder Technol.* **1983**, *19*, 11–19.
22. Klar, E.; Samal, P.K. Effect of density and sintering variables on the corrosion resistance of austenitic stainless steels. *Adv. Powder Metall. Part. Mater.* **1995**, *11*, 3–17.
23. Lei, G.H.; German, R.M. Corrosion of sintered stainless steels in a sodium chloride solution. *Mod. Dev. Powder Metall.* **1985**, *16*, 261–275.
24. Nyborg, I.; Tunberg, T.; Wang, P.X. Surface product formation during water atomization and sintering of austenitic stainless steel powder. *Met. Powder Rep.* **1990**, *45*, 750–753. [CrossRef]
25. Maahn, E.; Jensen, S.K.; Larsen, R.M.; Mathiesen, T. Factors affecting the corrosion resistance of sintered stainless steel. *Adv. Powder Metall. Part. Mater.* **1994**, *7*, 253–271.
26. Jones, F.M.F. The effect of processing variables on the properties of type 316L powder compacts. *Prog. Powder Metall.* **1970**, *30*, 25–50.
27. Lei, G.; German, R.L.; Nayar, H.S. Corrosion control in sintered austenitic stainless steels. *Prog. Powder Metall.* **1983**, *39*, 391–410.
28. Maahn, E.; Mathiesen, T. Corrosion properties of sintered stainless steel. In Proceedings of the U.K. Corrosion '91, Manchester, UK, 22–24 October 1991.
29. Dautzenberg, G.; Gesell, H. Production technique and properties of austenitic Cr-Ni stainless steel powders. *Powder Met. Int.* **1976**, *8*, 14–17.
30. Ashurst, A.; Klar, E. Mercury porosimetry. *Powder Metall. Met. Handb.* **1984**, *7*, 266–271.
31. Klar, E. Relationship between pore characterization and compacting properties of copper powders. *J. Mater.* **1972**, *7*, 418–424.
32. Pao, M.A.; Klar, E. Corrosion phenomena in regular and tin-modified P/M stainless steels. *Prog. Powder Metall.* **1984**, *39*, 431–444.
33. Samal, P.K.; Klar, E. Effect of sintering atmosphere on corrosion resistance and mechanical properties of austenitic stainless steels—Part I. *Adv. Powder Metall. Part. Mater.* **1997**, *2*, 14–55.
34. Raghu, T.; Malhotra, S.N.; Ramakrishnan, P. Corrosion behavior of porous sintered type 316L austenitic stainless steel in 3% NaCl solution. *Corrosion* **1989**, *45*, 698–704. [CrossRef]
35. Fontana, M.G.; Greene, N.D. *Corrosion Engineering*, 2nd ed.; McGraw-Hill Book Co.: New York, NY, USA, 1978.
36. Wilde, B.E. Influence of silicon on the pitting corrosion resistance of an 18Cr-8Ni stainless steel. *Corrosion* **1986**, *42*, 147–151. [CrossRef]
37. Bellezze, T.; Roventi, G.; Quaranta, A.; Fratesi, R. Improvement of pitting corrosion resistance of AISI 444 stainless steel to make it a possible substitute for AISI 304L and 316L in hot natural waters. *Mater. Corros.* **2008**, *59*, 727–731. [CrossRef]